

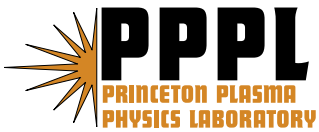
---

# Princeton Plasma Physics Laboratory

---

PPPL-

PPPL-



Prepared for the U.S. Department of Energy under Contract DE-AC02-09CH11466.

# Princeton Plasma Physics Laboratory

## Report Disclaimers

---

### Full Legal Disclaimer

This report was prepared as an account of work sponsored by an agency of the United States Government. Neither the United States Government nor any agency thereof, nor any of their employees, nor any of their contractors, subcontractors or their employees, makes any warranty, express or implied, or assumes any legal liability or responsibility for the accuracy, completeness, or any third party's use or the results of such use of any information, apparatus, product, or process disclosed, or represents that its use would not infringe privately owned rights. Reference herein to any specific commercial product, process, or service by trade name, trademark, manufacturer, or otherwise, does not necessarily constitute or imply its endorsement, recommendation, or favoring by the United States Government or any agency thereof or its contractors or subcontractors. The views and opinions of authors expressed herein do not necessarily state or reflect those of the United States Government or any agency thereof.

### Trademark Disclaimer

Reference herein to any specific commercial product, process, or service by trade name, trademark, manufacturer, or otherwise, does not necessarily constitute or imply its endorsement, recommendation, or favoring by the United States Government or any agency thereof or its contractors or subcontractors.

---

## PPPL Report Availability

### Princeton Plasma Physics Laboratory:

<http://www.pppl.gov/techreports.cfm>

### Office of Scientific and Technical Information (OSTI):

<http://www.osti.gov/bridge>

---

### Related Links:

[U.S. Department of Energy](#)

[Office of Scientific and Technical Information](#)

[Fusion Links](#)

# Dynamical Evolution of Pedestal Parameters in ELMy H-mode in the National Spherical Torus Experiment

A. Diallo<sup>1</sup>, R. Maingi<sup>2</sup>, S. Kubota<sup>3</sup>, A. Sontag<sup>2</sup>, T.  
Osborne<sup>4</sup>, M. Podestà<sup>1</sup>, R. E. Bell<sup>1</sup>, B. P. LeBlanc<sup>1</sup>, J.  
Menard<sup>1</sup>, and S. Sabbagh<sup>5</sup>.

<sup>1</sup>Princeton Plasma Physics Laboratory, Princeton University, NJ - USA

<sup>2</sup>Oak Ridge National Laboratory, Oak Ridge, TN - USA

<sup>3</sup>University of California, Los Angeles, CA - USA

<sup>4</sup>General Atomics, San Diego, CA - USA

<sup>5</sup>Applied Physics Department, Columbia University, New York, NY - USA

E-mail: [adiallo@pppl.gov](mailto:adiallo@pppl.gov)

**Abstract.** Characterizations of the pedestal parameter dynamics throughout the edge localized modes(ELM) cycles are performed on the National Spherical Torus Experiment (NSTX, [M. Ono et al., Nucl. Fusion 40, 557 (2000)]). A clear buildup of the pedestal height is observed between ELMs for three different plasma currents, which tends to saturate prior to the onset of ELM at low and medium plasma current. Similarly, the pedestal width increases with no clear evidence of saturation during an ELM cycle. The maximum pedestal gradient increases as a function of plasma current, reaches a nominal value after the ELM crash, and remains constant until the end of the ELM cycle. The pedestal height just prior to the onset of ELM is shown to increase quadratically with plasma current. The pedestal width  $\Delta$  is proportional to the square-root of the poloidal  $\beta$  at the top of the pedestal. Coherent density fluctuations strongly increasing at the plasma edge are observed to be maximum after the ELM crash and to decay during the rest of the ELM cycle. Finally, the pedestal parameters evolution during the ELM cycle as well as the scaling with  $I_p$  of the pedestal pressure prior to the onset ELM are found to be qualitatively consistent with the peeling ballooning theory.

## 1. Introduction

A successful operation of fusion reactors such as ITER [1] will require establishing a sufficiently high pressure at the top of the pedestal (referred to as pedestal height) during H-mode discharges. This is mainly due to the coupling between pedestal pressure and core fusion power. In addition, edge localized mode-(ELM)-induced energy loss must be restricted to less than 1% reductions of the pedestal stored energy in ITER to meet the heat load requirements on the plasma-facing-components (PFC) [2].

A defining feature of the H-mode is the existence, near the plasma boundary, of a transport barrier generating an H-mode pedestal. This pedestal can be quite narrow in width and is interpreted as the interface between two regions during high confinement(H-mode): the core plasma and the scrape-off-layer(SOL). These two regions are governed by different physical mechanisms inherent in the wide range of spatial and temporal scales and also in the presence of sources and sinks of particles. A large pedestal pressure has been found to improve the energy confinement, as seen in DIII-D [3] and JT-60U [4]. Predictions of the pedestal pressure required for a ratio of auxiliary heating to thermal power (i.e., Q) of 10 such as ITER is challenging without an accurate model of the edge pedestal and of its self-consistent coupling to the core plasma. Significant efforts have been undertaken in simulations using the multi-mode (MM), Weiland, IFS/PPPL, and GLF23 theory-based transport models (see Ref. [5] and references therein), which showed that the pedestal ion temperatures ( $T_i^{ped}$ ) required for achieving Q=10 in ITER range between 3 keV to 5 keV is compatible with ITER  $T_i^{ped}$  projections [6]. From the experimental point of view, significant research from multiple tokamaks looking into pedestal parameter scalings with plasma parameters are currently being undertaken and the current status and results of these experiments have been summarized in a review article [7].

It is well known that in ELMy H-mode, the core confinement and stored energy increase as the pedestal pressure and its gradient rise until a threshold, and therefore an upper-limit, is reached. This limiting threshold appears to be controlled by combinations of Magneto Hydrodynamic Dynamics (MHD) instabilities and transport physics. While there is no accepted transport mechanism explaining the residual electron heat transport in the pedestal, linear MHD through the peeling-ballooning

theory, however, provides a good description to the upper limit on the pedestal pressure.

The peeling-ballooning theory describes instabilities driven by both pressure and edge current gradients [8]. Based on this theory, the onset of an ELM is driven by a critical pressure gradient ( $\nabla p_{crit}$ ) at a given pedestal width, which in turn peaks the bootstrap current. Making the assumption that the maximum pedestal pressure (resulting in an upper-limit) can be written in terms of the pedestal width  $\Delta_p$  and critical pressure gradient as  $\Delta_p * \nabla p_{crit}$ , one can argue that one aspect of the peeling ballooning theory effectively provides the maximum pedestal height which is more accurately quantifiable than  $\nabla p_{crit}$  prior to the onset of ELM. The other aspect of the peeling-ballooning theory is related to the edge current gradient. In addition to the local parameters (e.g.,  $\nabla p_{crit}$ ), the peeling-ballooning theory is sensitive to the radial extent of the associated modes, and the overall size of the pedestal. The upper limit of the pedestal pressure is thought to be reached just prior to the onset of an ELM. Once an ELM is triggered, filamentary bursts [9] of energy and particles are transported from the vicinity of the pedestal to the SOL thereby relaxing the pedestal pressure and edge current gradients to a stable regime. We refer to pedestal height as the total thermal (ion and electrons) pressure at the top of the pedestal ( $P_{ped}$ ).

Recent DIII-D [10, 11] results from a model study based on the peeling-ballooning theory showed that the pedestal width scales with the pedestal poloidal beta  $\beta_\theta^{ped} = 2\mu_0 P_{ped}/B_\theta^2$ . Here  $B_\theta = \mu_0 I_p/L_p$  is the averaged poloidal magnetic field at the pedestal top and  $L_p$  the circumference of the last closed flux surface. In the experiments testing the model, the pedestal width was approximated as  $(\Delta_{ne} + \Delta_{Te})/2$ , where  $\Delta_{ne}$  and  $\Delta_{Te}$  represent electron density and temperature widths, respectively. ASDEX Upgrade [12], on the other hand, found that  $\Delta_{ne}$  is independent of  $\beta_\theta^{ped}$  and the  $\Delta_{Te}$  scaling with  $\sqrt{\beta_\theta^{ped}}$  cannot be excluded within error bars. The latter correlation appears to be consistent with observations from other tokamaks. More specifically, on JT-60, Urano and co-workers [13] found through mass scans using Hydrogen and Deuterium that the pedestal width scales with  $\rho^{*0.2} \sqrt{\beta_\theta^{ped}}$ . Here  $\rho^* \propto T_i^{ped}/aB_\theta^{ped}$  ( $a$  is the minor radius). MAST has reported similar scalings where  $\Delta_{Te}$  scaled weakly with  $\rho^*$  but correlated with  $\sqrt{\beta_\theta^{ped}}$  [14]. The above observations from multiple tokamaks show a mix of trends in the pedestal height-width scalings, which suggests the existence of hidden variables. Extension of these

scalings to low aspect-ratio tokamaks for wider parameter coverage, as well as the addition of fluctuation measurements during the ELM cycle, are needed for a deeper understanding of the pedestal structure dynamics.

The H-mode pedestal in National Spherical Torus Experiment (NSTX) was first described in the work of Maingi and co-workers [15]. In that work, analysis of the pressure profiles in NSTX showed that the pedestal stored energy represents between 25% and 33% of the total plasma stored energy. Furthermore, the pedestal stored energy was found to agree with the multi-machine scaling relation reported in Cordey [16]. In NSTX, multiple intrinsic ELMs ranging from large to small have routinely been observed [15]. The size of ELMs is typically given as the ratio of ejected stored energy to either the pedestal or the total stored energy. Giant type I ELMs can eject up to 30% of the stored energy. Small ELMs (type V see Ref. [17]), however, have less than 1% effects on the total stored energy making them difficult to measure via equilibrium reconstructions.

All the previously quoted research on NSTX was performed with boronized carbon PFCs. Recently lithiumization was introduced as a wall conditioning technique. Lithium evaporations on part of the PFC walls have resulted in reductions in the frequency and amplitude of ELMs [18], including complete ELM suppression for periods of up to 1.2 s, ascribed to modification of the edge stability [19]. There is a minimum amount of lithium required for complete ELM suppression. For lithium evaporation below this minimum amount, ELMs are still observed. Thus, to access ELM regimes and to insure discharge reproducibility, low levels of Li coating (< 100 mg) are typically applied to the bottom divertor between discharges in this set of experiments.

In this work, we first show evolution of the pedestal parameters (e.g., height, width, gradient) during an ELM cycle as a function of plasma current  $I_p$  at constant plasma shaping with toroidal magnetic field  $B_\varphi$  varying within 10%. Then we show the total pedestal pressure scales with  $I_p^2$ . In addition, the pedestal width scales with  $\sqrt{\beta_\theta^{ped}}$ . These scalings provide a good description of NSTX data over a wide range of  $I_p$ . Finally, we examine correlations between the pedestal width and edge fluctuations. More specifically, we analyze the density fluctuations near the plasma edge during an ELM cycle, and compare the fluctuation levels with pedestal width evolution. Initial results show that these density fluctuations appear to be uncorrelated with the ELM

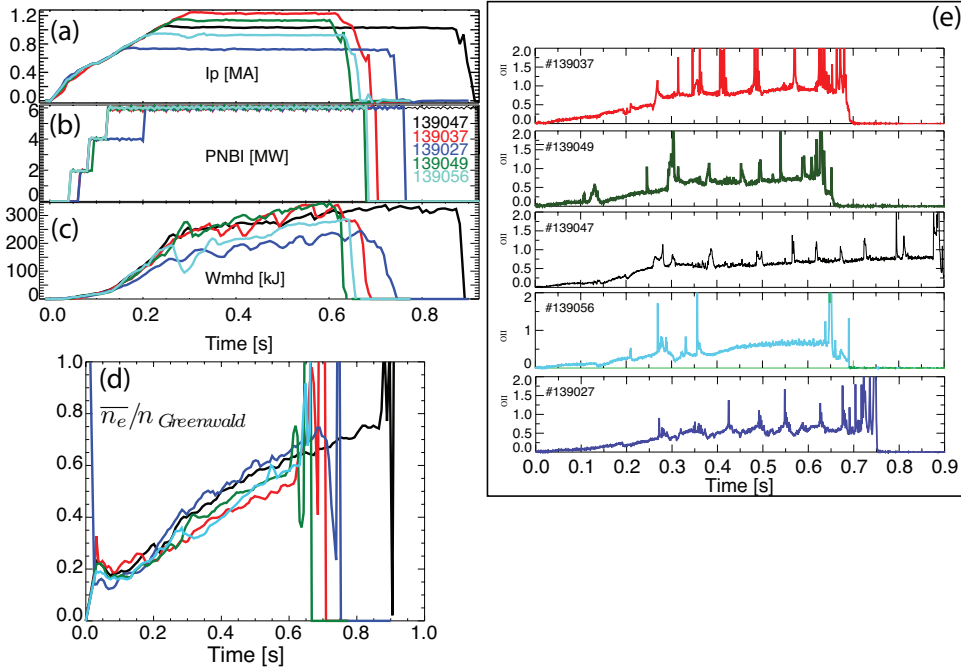


Figure 1: (color online) Discharges characteristics: (a) Plasma Currents. (b) Injected power. (c) Total stored energy showing dips associated with ELMs. (d) The Greenwald density fraction. (e) Divertor O-II signals clearly showing ELMs. Note the divertor O-II signals can be use in *lieu* of the  $D_\alpha$ .

cycle.

The remainder of this paper is organized into four sections. Section 2 describes the experimental details and the profile analysis techniques needed to systematically obtain the pedestal structure scaling results. Evolution of the pedestal parameters during an ELM cycle and scalings with global parameters are discussed in Section 3. Analysis of Fluctuations during an ELM cycle is presented in section 4. Finally, section 5 presents a summary.

## 2. Experimental Description and Profile Analysis Technique

Experiments were carried out on the NSTX, a medium-sized low aspect-ratio spherical torus (ST) of major radius  $R \sim 0.85$  m, minor radius  $a \leq 0.67$  m, and  $B_\phi \leq 0.55$  T. The experiments described here are performed using Neutral Beam Injection (NBI) heating with power ranging from 4MW to 6 MW. The discharges studied use a marginally

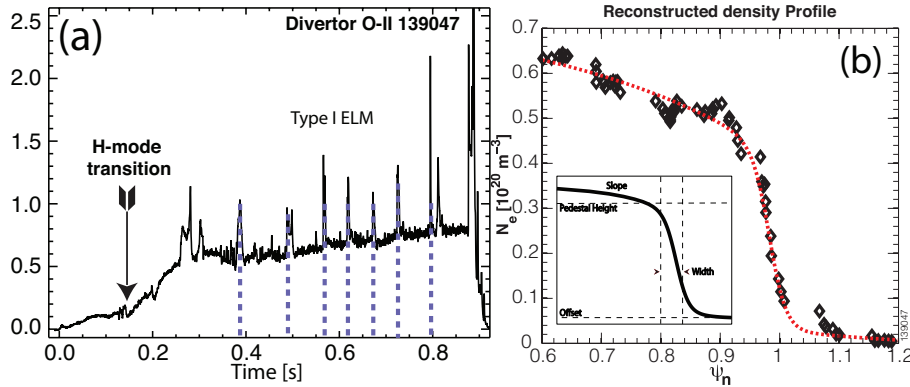


Figure 2: (a) The divertor O-II signals with large Type I ELMs. The dashed vertical bars indicate the ELM times. (b) Example of a composite profile, in normalized flux  $\psi_n$ , of the electron density associated with Type I ELM in (a). Diamonds represent the data points and the broken line the best fit using a modified hyperbolic tangent. The inset figure illustrates the parametrization. Typical vertical error bars  $\sim 5\%$ . Larger error bars occur in the far SOL.

double-null divertor configuration, with the plasma slightly biased down ( $\delta_r^{sep} \sim -5$  mm, where  $\delta_r^{sep} \sim$  is the radial distance between the two X-points mapped to the outer midplane), and the bottom triangularity  $\delta_{bot} \sim 0.6$ . The upper triangularity was typically kept at 0.4 and the elongation  $\kappa$  was kept between 2.3 and 2.4. Figure 1 shows the NBI power,  $I_p$ , total stored energy ( $W_{mhd}$ ), and divertor O-II (proxy for the  $D_\alpha$ ) signals of the discharges examined in this paper. The shape parameters (e.g.,  $\delta$ ,  $\kappa$ ) were held constant and the magnetic field was varied from 0.5 T to 0.55 T. To target ELMy discharges for studies reported here, a total of 50 mg of lithium was deposited on the bottom divertor plates between discharges. The key diagnostics utilized to characterize the pedestal parameters are the mid-plane Thomson scattering system for  $n_e$  and  $T_e$  sampled at 60 Hz [23], the  $C^{6+}$  charge-exchange recombination spectroscopy [24] for providing the carbon density and ion temperature  $T_i$  with a 10 ms time resolution, and the divertor  $O-II$  and the  $D_\alpha$  filter scopes for identifying ELMs. In this work, we use the divertor  $O-II$  signal instead of the  $D_\alpha$ .

In this work, analysis of the evolution of the pedestal structure during an ELM cycle is presented. We characterize the evolution of the radial profiles between ELMs



by reconstructing composite profiles synchronously with multiple ELMs. Here, we focus on type I ELMs of typical frequency ranging between 20 Hz and 70 Hz and characterized by large spikes on the divertor O-II signal as indicated in figure 2(a). The radial profiles of density, temperature and consequently the pressure are first mapped in normalized poloidal flux coordinates [ $\psi_n = (\psi_c - \psi)/(\psi_c - \psi_{sep})$ ], where  $\psi_c$  and  $\psi_{sep}$  represent the flux at the core and at the separatrix, respectively], and then collected during inter-ELM periods: this can be regarded as a correlated sampling approach. The equilibrium reconstruction has a 10 ms time resolution, however for the purpose of the profile reconstruction, the equilibrium is down-sampled to match the Thomson scattering sample frequency (i.e., 60 Hz).

An example of this correlated sampling for the  $n_e$  profile is shown in figure 2 (b) where the dashed line represents the best fit using a modified hyperbolic tangent function that parametrizes the pedestal height and width [25]. This widely used analytic function fits the steep gradient region in the pedestal, reduces sensitivity to noise in individual data points, and provides a systematic way to represent pedestal structure [26]. The electron profiles ( $n_e$  and  $T_e$ ) are fitted using a modified hyperbolic tangent defined as:

$$\frac{\alpha - \alpha_0}{2} \frac{(1 - a_1 \zeta)e^\zeta - e^{-\zeta}}{e^\zeta + e^{-\zeta}} + \frac{\alpha + \alpha_0}{2}.$$

where  $\alpha$  and  $\alpha_0$  represent the pedestal height and the offset (shown in the inset of figure 2), respectively.  $\zeta = 2(\psi_n^{sym} - \psi_n)/\Delta$ ,  $\psi_n^{sym}$  and  $\Delta$  represent the symmetry point and the width, respectively. The ion profiles exhibit less of steep gradients than the electron profiles and hence cannot be fitted using the modified tanh function. They are adequately fitted using cubic splines.

The profile fits are performed around sliding temporal windows of 20% width to capture details of the inter-ELM dynamics. For example, we represent a window between 30% and 50 % of an ELM cycle by its midpoint, which in this case is 40%. With this defined proxy,  $n_e$  or  $T_e$  *prior to* and *after* an ELM crash are identified as 90% and 30% of an ELM cycle, respectively. On average three profiles are used to constrain each sliding window. Figure 3 shows examples of profiles for ions and electrons with associate fits (from  $\psi_n = 0.7$ ), where the electron pedestal density, temperature, and subsequently pressure are higher prior to the onset of ELMs than just after, which clearly indicates an increase of the total pressure prior to the onset of an ELM. In

In addition, we observe an inward shift of the top of the pedestal hinting at an increase of the pedestal width. For the remainder of the text, the pedestal parameters refer to those of the total pressure derived using a composite of  $n_e$ ,  $T_e$ ,  $n_i$ ,  $T_i$  profiles. This composite is subsequently fit using the modified tanh function given in the above equation. The resulting fit yields an estimate of the pedestal width ( $\Delta$ ) from which a gradient ( $\alpha/\Delta$ ) can be determined. The error in the fit in combination with an estimate of the scatter around the fit yields estimates on the error of the pedestal parameters.

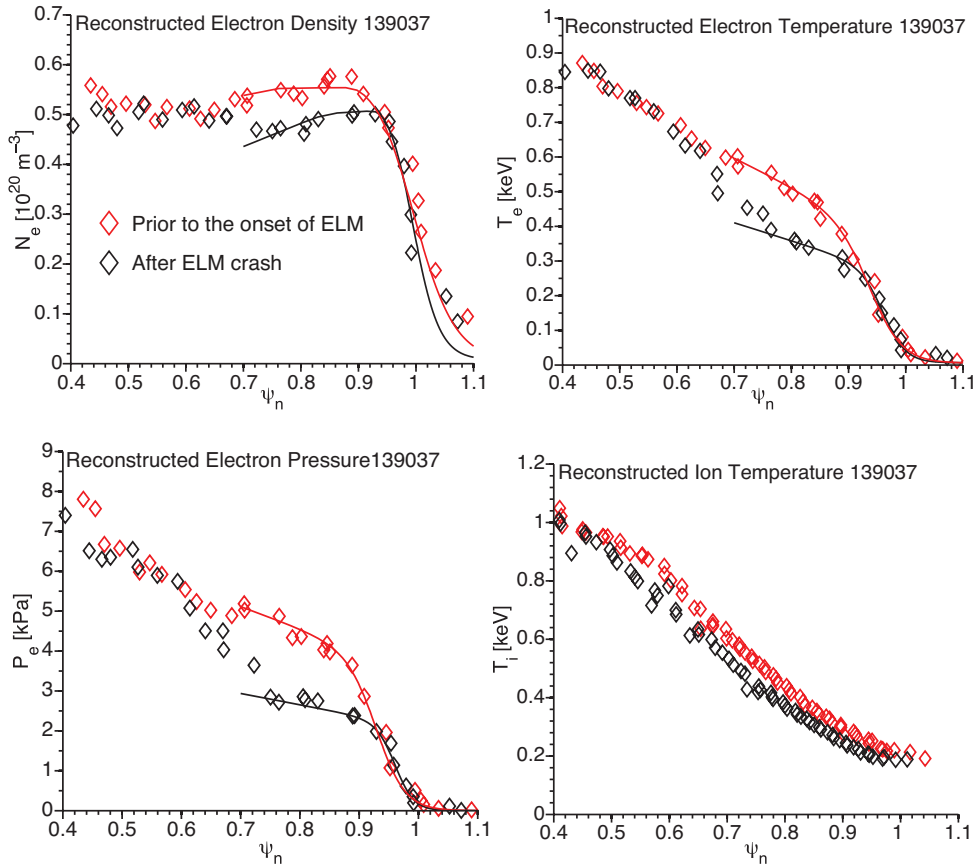


Figure 3: (color online) Example of ELM based reconstruction profiles prior to the onset and after an ELM: (a) electron density; (b) electron temperature; (c) electron pressure; and (d) ion temperature. Error bars in the range of 3% are typical for  $n_e$ , and in range of 4% to 5% for  $T_e$  and  $P_e$ .

### 3. Pedestal structure evolution during an ELM cycle and scaling studies

Based on linear ideal MHD stability theory, it has been suggested that ELMs are associated with both ballooning [27] and kink or peeling modes [28, 29], or of their coupling referred to as peeling-ballooning modes [30, 8]. The latter mode taps its free energy from both the pressure gradient and the current density [8]. NSTX ELMY discharges, however, have been shown to be kink/peeling unstable [21, 20, 22]. ELMs are thought to be triggered at a critical pedestal pressure gradient or edge current gradient. In this section, we show results of measurements of the pedestal structure on NSTX for various  $I_p$  during an ELM cycle.

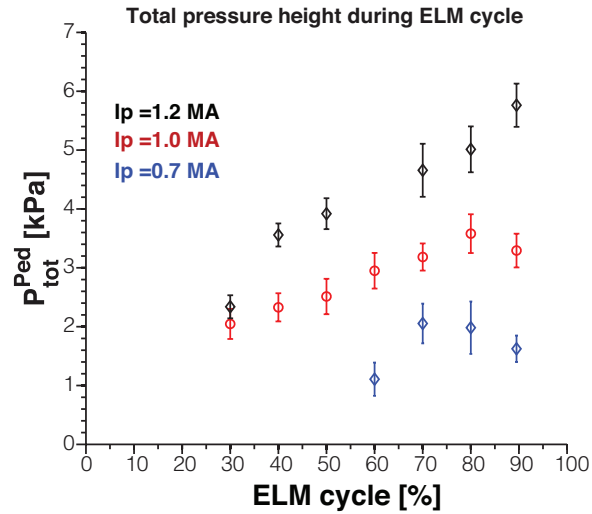


Figure 4: (color online) Total pressure buildup during ELM cycle, for three cases of  $I_p$ ; all other parameters are kept constant. The ELM frequency ranges from 20 Hz to 70 Hz.

*Pedestal parameters evolution through an ELM cycle:* The total pressure (i.e., ions and electrons) evolution at the top of the pedestal during various stages of an ELM cycle for three cases of plasma current is shown in figure 4. The ELM frequencies vary between 20 Hz and 70 Hz with no systematic trend as a function of  $I_p$ . We observe a clear buildup of the pedestal pressure before the onset of ELMs for these cases (low, medium, and high  $I_p$  all at the same toroidal field  $\sim 0.5$  T) similar to observations in MAST [31] and AUG [32]. In the low and medium  $I_p$  cases, we observe a saturation

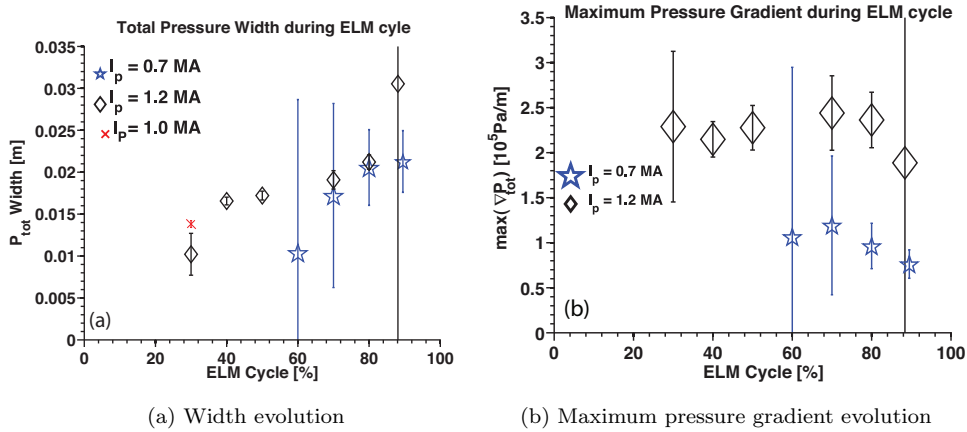


Figure 5: (a) Pressure width evolution during an ELM cycle for three values of plasma current. Stars ( $\star$ ) indicate the low plasma current value; the diamond ( $\diamond$ ), the high plasma current case, and the cross ( $\times$ ) the medium current case. (b) The maximum pressure gradient for the low and high current case stays constant during an ELM cycle.

late in the ELM cycle of the pedestal height in contrast to the high current case where the pedestal height increases until the onset of the ELM. In addition, figure 4 shows a factor of three increase in pedestal height during the ELM cycle for the high plasma current case: this is similar to DIII-D where a factor of four increase of the inter-ELM pedestal pressure was observed [33]. The saturation late in the ELM cycle contrasts observations in DIII-D [33] where the electron pedestal pressure saturates in the early phase, e.g., 20% - 50% of the ELM cycle.

Figure 5(a) indicates, for the case of  $I_p = 1.2$  MA and to a lesser extent for the case of 0.7 MA, that the pedestal width increases until the onset of an ELM to a nominal value of  $\sim 2$  cm ( $0.085[\psi_n]$ ). For the medium  $I_p$  case, only one point is included in the early stage of the ELM cycle as the remaining points have error bars too large to allow for meaningful comparison. We note that the widening of the pedestal during the ELM cycle is qualitatively consistent with the phenomenology of transport barrier inward expansion [34, 35]. An analytic model based on this phenomenology predicts that the rise of the pedestal width results from inward propagation from the edge of the pedestal pressure front into the core plasma [34], which implies an increase of

the pedestal pressure width.

Figure 5(b) shows the maximum pressure gradient for various parts of an ELM cycle. There is an increase of the maximum pressure gradient with  $I_p$ . Furthermore, we observe that maximum pressure gradient remains constant within error bars during the ELM cycle. This lack of variation in the maximum pressure gradient is consistent with recent observations in both AUG [36] and DIII-D [33, 7], where the maximum pressure gradient initially increases and is limited at an early phase of the ELM cycle. In our case, the increase of the pressure prior to its saturation [before the 20% of the ELM cycle] could not be resolved. Hence, in view of this saturation prior to the ELM crash, the pressure gradient appears to play a weak role in the triggering of an ELM. In the framework the peeling-ballooning physics, it is conceivable that the edge current could play a role just prior to the ELM crash.

Thus, we have shown that the pedestal maximum is a limit and can hypothesize the critical gradient is recovered very soon after the ELM crash leaving the pedestal height and width, and the edge current as key players in the onset of the ELMs. Observations of the pedestal height evolution for various plasma currents are consistent with observations made in high R/a tokamaks such as DIII-D [37], and provide additional opportunities for extending predictive pedestal structure models to ST.

*Pedestal width scaling with plasma current, magnetic field, and poloidal  $\beta$ :*

Correlations between the pedestal width and  $\beta_\theta^{ped}$  have been observed on many tokamaks (e.g., JT60U [4], MAST [14], and see ref. [38] for DIII-D and C-MOD). Independent correlations, however, between the width and  $\rho^*$  and width and  $\beta_\theta^{ped}$  have been difficult to assess. In JT60U, to separate the dependence between  $\rho^*$  and  $\beta_\theta$ , experiments in hydrogen and deuterium were carried out keeping  $\beta_\theta$  and  $\nu^*$  fixed in type I ELMy discharges. It was found that the pedestal width dependence on  $\rho^*$  is weak and that the ion temperature pedestal width was found to scale with  $\rho^{*0.2}\sqrt{\beta_\theta^{ped}}$  [13] and similar results on the pedestal width (i.e.,  $(\Delta_{Te} + \Delta_{Ne})/2$ ) in DIII-D [10] showed a weaker dependence in  $\rho^*$  but scaling with  $\sqrt{\beta_\theta^{ped}}$ . The DIII-D pedestal width scaling was observed to be in agreement with the EPED predictive model (the reader is referred to Snyder and coworkers [39] for details on the EPED model). EPED combines a pedestal width constraint, based on expectations from the onset of strong electromagnetic kinetic ballooning mode (KBM) turbulence near

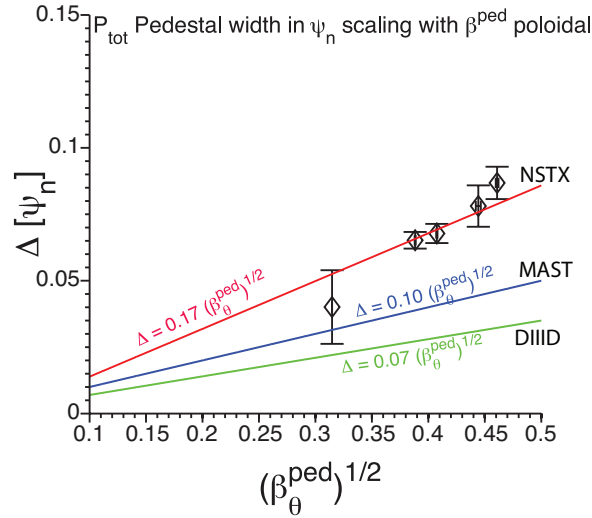


Figure 6: The pedestal width in  $\psi_n$  scaling with the pedestal poloidal  $\beta$  and the associated best fit. This width scaling effectively provided a relation between the width and the height of the pedestal (see text for details). Shown also are the fits for MAST and DIII-D for comparison.

a critical value of the pressure gradient, with peeling-ballooning stability to yield a predictive model on the pedestal height and width. Furthermore, the onset of the KBM leads to a weak or no dependence of the width on other normalized parameters inherent to the KBM dispersion relation.

In NSTX, we observe no systematic trends between the pedestal width and  $\rho^*$  (evaluated at the electron pedestal temperature), which is not inconsistent with the KBM arguments. On the other hand, figure 6 shows a clear dependence of the pedestal width prior to the type I ELM onset (e.g., the last 20% of an ELM cycle) of type I ELM on  $\beta_{\theta}^{\text{ped}}$ . The width scales with  $\sqrt{\beta_{\theta}^{\text{ped}}}$ , with a best fit equation being  $\Delta = 0.17(\beta_{\theta}^{\text{ped}})^{1/2}$ . This pedestal width correlation of the type “ $\Delta = c(\beta_{\theta}^{\text{ped}})^{1/2}$ ” is consistent with experimental observations in DIII-D and MAST, except the fitting coefficient  $c$  in NSTX is slight larger than that of MAST [14] and 2.4 times greater than that of DIII-D [10]. In summary, the coefficient appears to be overall larger in ST than in high aspect ratio tokamaks pointing to a different type of coupling of the pedestal width and height in STs. The difference in values of  $c$  in STs remains unclear. Furthermore, this scaling provides the necessary ingredients for testing EPED in ST.

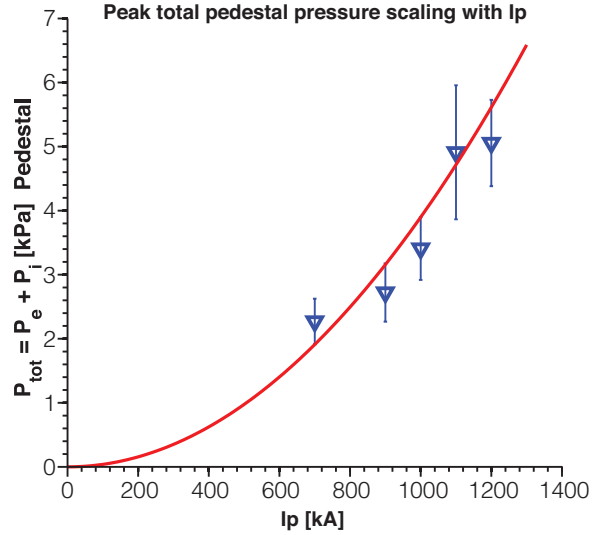


Figure 7: Pedestal height scaling with  $I_p$ : collecting the pedestal pressure at the onset of ELMs, we show that the pedestal height scales with  $I_p^\alpha$ , where  $2.0 \leq \alpha \leq 2.6$  with a reduced  $\chi^2 \sim 0.63$

Note that EPED was initially developed for large aspect-ratio tokamaks. Test of a version of EPED supporting low aspect-ratio tokamaks will be the subject of future work.

To further characterize the pedestal, we examine the total pedestal pressure dependence with global parameters such as  $I_p$ . We compile the total pedestal pressure during the last 20% of an ELM cycle. Figure 7 shows a near quadratic (within error bars) increase of the pedestal height prior to the ELM onset (e.g., 90% ELM cycle) with  $I_p$ . Note that the toroidal field was 10% higher for  $I_p = 900$  kA and 1.1 MA than that of  $I_p = [1.2, 1.0, 0.7]$  MA.

Initial test of the effects of  $B_\phi$  on this scaling showed limited effects on the pedestal height. The test was performed over a small range of  $B_\phi$  with ELMy discharges and a larger range of ELM-Free discharges, where no discernible effects on the pedestal height could be found. A more stringent test will be performed using a much larger set of ELMy discharges to be obtained over a wider range of  $B_\phi$  in future experimental campaign.

The above scaling studies show that  $I_p$  has a dominant effect in determining the pedestal height compared to  $B_\phi$ . Similar scaling consistent with  $I_p^2$  scaling has been

observed in CMOD [40] on the “Enhanced  $D_\alpha$ ” H-mode datasets. DIIID, however, has reported a linear scaling of the electron pedestal height with  $I_p$  (see fig.3(c) in Ref. [37]), which can arguably change once the ion pedestal height is included. The  $I_p^2$  dependence of the pedestal pressure has been suggested by Lingertat and coworkers [41] as a manifestation of the ballooning instability. While such scaling is expected in JET [42] discharges, recent NSTX stability analysis using ELITE [43, 44] have shown that ELMy discharges are at the kink/peeling boundary [21]. Similarly, on CMOD, stability analyses have demonstrated operation above the ballooning stability limit, even though the pedestal scaling with  $I_p^{2 \leq \alpha \leq 2.6}$  was also observed. The discrepancy between stability analysis and observed scaling as a manifestation of ballooning instability points to the existence of other mechanisms (e.g., transport) playing a role.

#### 4. Density fluctuations analysis during an ELM cycle

The characterization of the evolution of the density fluctuations during an ELM cycle is motivated by recent hypothesis where it was proposed that the onset of a KBM near a critical value of the pressure gradient sets the pedestal width [39]. This ballooning type mode is predicted to have its real frequency near  $\omega_{pi}^* \sim 30$  kHz [45] assuming  $k_\theta \rho_i$  in the vicinity of 0.3, and with  $\omega_{pi}^* = 0.5 k_\theta \rho_i v_{thi} / L_{ni} (1 + \eta_i)$ . Here,  $L_{ni}$  is the ion density gradient scale length,  $v_{thi}$  is the ion thermal velocity, and  $\eta_i$  the ratio of density to temperature scale lengths. Recent gyrokinetic simulations of a representative NSTX high-beta discharge have shown the transition between distinct ITG and KBM modes to an hybrid ITG/KBM mode at large pressure gradient [46] and at  $r/a = 0.7$  further motivating the need to identify the KBM experimentally. KBMs are hypothesized to set the pedestal gradient, which in turn constrains both the pedestal width and height. To qualitatively test this hypothesis, we investigate correlations between the pedestal structure evolution and density fluctuations.

The density fluctuations at various stages of an ELM cycle are obtained using the 16-channel reflectometer probing the edge plasma [47]. From the complex signal (in-phase and quadrature), one obtains the phase fluctuations which can in principle be related to local density fluctuations (see Ref. [48] for a review). We then conditionally sample, based on the ELM cycle, the deduced phase signal for each channels. The



resulting signal is decomposed into temporal segments of an ELM cycle (e.g., 20%–40%). Such decomposition insures that  $n_e$  measurement points are included in each temporal segment and independently for each channel.

In order to extend the analysis to the frequency domain, we cross-correlate pairwise the segments corresponding to the same ELM cycle for various ELMs, and then apply a Fourier transformation. This approach eliminates uncorrelated fluctuations and yields a cross-power spectrum of the phase fluctuations. In addition, we average over all the ELMs present in the discharges, which further suppresses the noise ( $1/\sqrt{N}$ ,  $N$  is the number of ELMs) to enhance the correlated components. A similar approach was successfully implemented in Diallo and Skiff [49] to pull a kinetic component of weak amplitude out of fluctuation spectra dominated by drift waves. The resulting phase fluctuation spectra are mapped into  $\psi_n$  space using the electron density fit (see figure 8(d-f)) and the reflectometer cutoff densities.

To estimate the local density fluctuations based on the phase fluctuations, we assume a 1D geometric optics approximation [48] where  $k_r L_n \leq 1$ , which is a reasonable assumption for the edge of the tokamak. Given this assumption, the phase fluctuation  $\delta\varphi$  corresponds approximately to  $\sim 2k_0 L_n \delta n_e / n_e$  as described in Ref. [48]. Here  $L_n$  is the density scale length computed from density profiles in figure 8(d-f), and  $k_0$  the vacuum wavenumber at the cutoff densities. Figures 8(a-c) show contour plots of the cross-power spectra of the density fluctuations during the early-, mid-, and late- phases of the ELM cycle. Most of cross-power spectra are localized toward the region of strong density gradients. Furthermore, the fluctuations, estimated using the phase fluctuations, increase at the very edge of the plasma away from the peak density gradients (see figure 9). Due the lack of reflectometer measurements in the SOL, it remains unclear if this increase of the fluctuations away from the peak density gradient can be ascribed to edge transport barrier phenomenon or if the increased levels of fluctuations continue into the SOL. Note a slight radial shift between the peak density gradient and the maximum density fluctuations, which we attribute to misalignment due to the equilibrium reconstructions.

The observed density fluctuations exhibit a coherent peak in the vicinity of 12 kHz at the edge of the density. The overall fluctuation level decreases prior to the onset of ELM. The characteristics of the 12 kHz coherent fluctuation observed in the density fluctuations could not be attributed to modes detected on the Mirnov signals

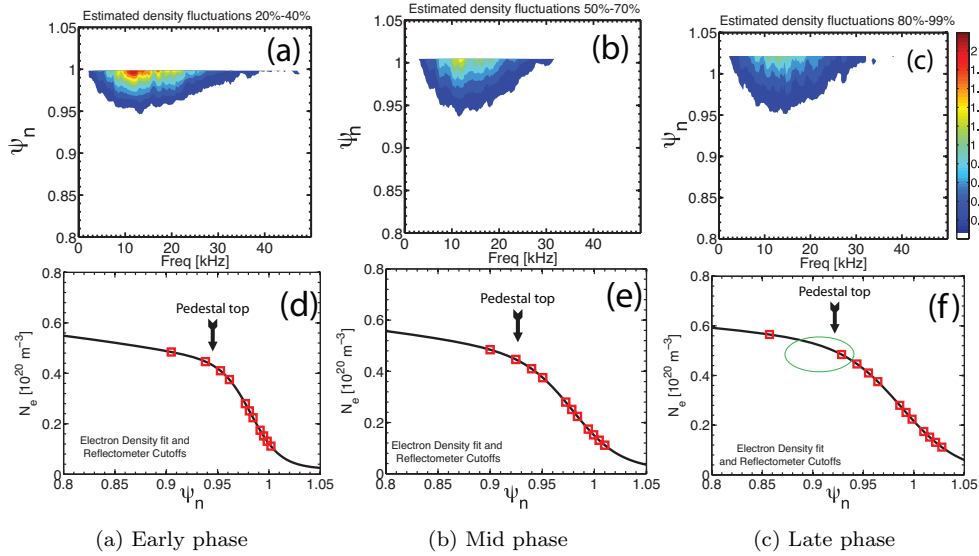


Figure 8: (color online) Estimated density fluctuations contour plots during the ELM cycle with associated density profiles during three phases of the ELM cycle for the medium plasma current case ( $I_p = 1.0$  MA). The same colorbar scale is used for all three contour plots. The bottom row shows the density profiles with the squares indicating the reflectometer probing locations and the arrows pointing to the top of the pedestal.

as shown in figure 10, which indicates that either the peak density fluctuation spectra are too weak to be detected by Mirnovs or that they are electrostatic.

From the constant pressure gradient during the ELM cycle observed in figure 5(b) for the other two cases ( $I_p = 1.2$  MA and  $I_p = 0.7$  MA), one might conclude the fluctuation level provided by the pressure gradient drive remains constant during the ELM cycle. This, however, is not reflected in the observed density fluctuations. One can speculate that the quenching of the density fluctuations lead to a reduction of the particle transport during the ELM cycle which is not inconsistent with a pedestal build up during ELM cycle. Nonetheless, the observed fluctuations suggest that they are not likely to play a role in constraining the profiles inside the edge barrier.

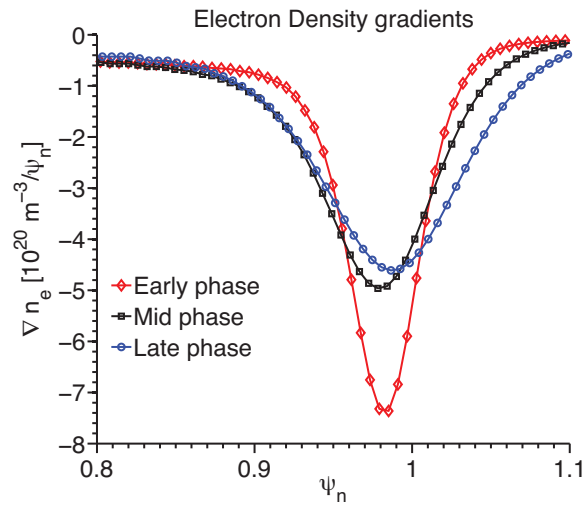


Figure 9: (color online) Density gradients obtained from fits during the three ELM phases for  $I_p = 1.0$  MA.

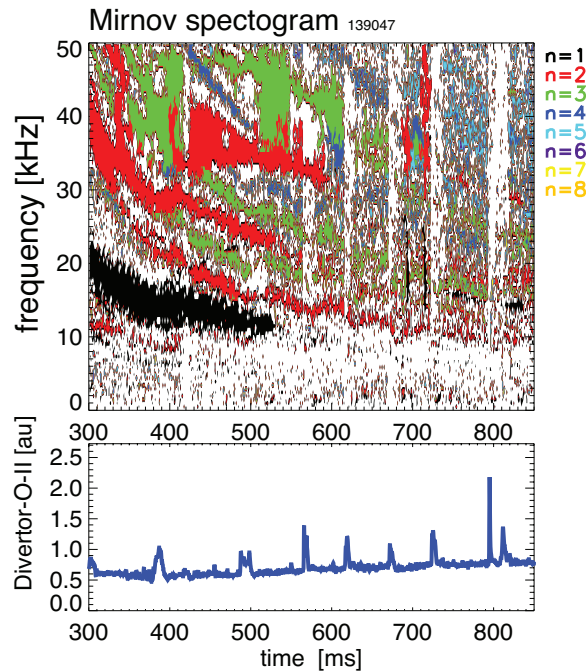


Figure 10: (color online) Top: signature of MHD activities using spectrograms from Mirnov coils with associated  $n$ -number modes. Below: corresponding divertor O-II signals showing the ELM events.

## 5. Summary

In this work, we provide detailed analysis of the dynamical evolution of the pedestal parameters in NSTX NBI heated discharges with type I ELMs. Analyses of scans in  $I_p$  and  $B_\varphi$  at constant shape during ELM cycle have been performed. We have shown that the pedestal height and width increase during ELM cycles qualitatively consistent with the peeling ballooning theory. The maximum gradient of the total pressure remains constant throughout the ELM cycle once a nominal gradient ( $\nabla p_{crit}$ ) is recovered immediately after the ELM crash. The saturation at  $\nabla p_{crit}$  early in the ELM cycle clearly indicates that the pressure gradient is unlikely a key player in triggering ELMs. Coupled with the saturated gradient is an increase of the pedestal width, which is known to be destabilizing. Assuming the peeling ballooning theory as working model for the ELM triggering both the width expansion and edge current gradient are candidates for the triggering of the ELMs.

The pedestal height was found to scale with  $I_p^2$  similar to CMOD observations [40]. Such  $I_p^2$  dependence appears to be a manifestation of the ballooning instability [41], which would suggest that the pedestal height scaling can be ascribed to the ballooning stability. In addition, the  $I_p^2$  scaling of the pedestal height is clearly favorable for higher current machine and bodes well in NSTX Upgrade where  $I_p$  is projected to reach 2 MA.

The pedestal width  $\Delta$  is found to scale as  $\Delta = c \sqrt{\beta_\theta^{ped}}$  ( $c = 0.17$  in NSTX) exhibiting qualitative similarity with the EPED model, and the DIII-D [10] ( $c = 0.06$ ) and MAST [14] ( $c = 0.13$ ) experimental observations. The general width scaling with  $\sqrt{\beta_\theta^{ped}}$  is consistent with the barrier expansion phenomenology and shows that in ST this expansion is more pronounced than higher aspect ratio tokamaks such as DIII-D. The characterization of the pedestal parameters during an ELM cycle provide a good description of the NSTX ELMy regimes over a wide range of plasma current and will be used for future tests of predictive pedestal models, such as EPED.

We examined the density fluctuations measured at the plasma edge during multiple ELM cycles using a 16-channel reflectometer. We observe large coherent fluctuations (near 12 kHz) increasing at the very edge of the plasma and away from the maximum density gradient. The coherent fluctuation decreases during prior to the onset of the ELM cycle and is not observed in Mirnov spectrograms (suggesting that

the coherent peak might be electrostatic). In summary, the behavior of the density fluctuations suggests that they are less likely to play a role in constraining the profile gradients inside the edge barrier as the pedestal builds up.

The above experimental studies of the dynamic of pedestal parameters over a wide engineering parameters space provide predictions on the performance of NSTX U. For instance scaling of the height and increase of the width with  $I_p$  will yield a factor 2.7 increase of the total pedestal pressure for NSTX U as well as a significant rise in the pedestal width, which will be manifested in higher pedestal stored energy. In addition to the predictive capability of next generation ST, results from these studies will be used for testing the pedestal structure predictive models which will be the subject of future articles.

### Acknowledgments

NSTX team is gratefully acknowledged. A. D. acknowledges fruitful discussions with P. Snyder. We would like to thank the referees for their constructive comments. Work supported by US DOE contract no. DE-AC02-09CH11466, DE-AC05-00OR22725, DE-FG03-99ER54527, DE-FC02-04ER54698, and DE-FG02-99ER54524.

- [1] ITER Physics Basis Editors, Nucl. Fusion **39** (1999) 2137.
- [2] LOARTE, A. et al. in Fusion Energy 2008 (Proc. 22nd Int. Conf. Geneva, 2008) (Vienna: IAEA), in <http://www-naweb.iaea.org/napc/physics/FEC/FEC2008/html/index.htm> .
- [3] OSBORNE, T. H., GROEBNER, R. J., LAO, L. L., et al., Scaling of ELM and H-mode pedestal characteristics in ITER shape discharges in the DIII-D tokamak Europhysics Conf. Abstracts, Proc. 24th EPS Conf. on Controlled Fusion and Plasma Physics (Berchtesgaden, Germany, 1997) vol 21A ed W. Schittenhelm et al (France: European Physical Society) pp 1101-5 part III,
- [4] URANO, H., KAMADA, Y., SHIRAI, H., et al., Nuclear Fusion **42** (2002) 311.
- [5] MUKHOVATOV, V., SHIMOMURA, Y., POLEVOI, A., and ET AL., Nucl. Fusion **43** (2003) 942.
- [6] M Shimada et al. Progress in the ITER Physics Basis Chapter 1: Overview Nucl. Fusion 47 (2007) S1.
- [7] MAGGI, C. F., Nucl. Fusion **50** (2010) 0660001.
- [8] CONNOR, J. W., HASTIE, R. J., WILSON, H. R., and MILLER, R. L., Phys. of Plasmas **5** (1998) 2687.
- [9] KIRK, A., WILSON, H. R., COUNSELL, G. F., et al., Phys. Rev. Lett. **92** (2004) 245002.
- [10] GROEBNER, R., LEONARD, A., P.B. SNYDER1, T. O., et al., Nucl. Fusion **49** (2009) 085037.

- [11] SNYDER, P. B., GROEBNER, R. J., LEONARD, A. W., OSBORNE, T. H., and WILSON, H. R., *PHYSICS OF PLASMAS* **16** (2009).
- [12] MAGGI, C., GROEBNER, R., ANGIONI, C., et al., *Nucl. Fusion* **50** (2010) 025023.
- [13] URANO, H., TAKIZUKA, T., KAMADA, Y., et al., *Nucl. Fusion* **48** (2008).
- [14] KIRK, A., O'GORMAN, T., SAARELMA, S., et al., *Plasma Physics and Controlled Fusion* **51** (2009) 065016.
- [15] MAINGI, R., BUSH, C., FREDRICKSON, E., and ET AL., *Nucl. Fusion* **45** (2005) 1066.
- [16] CORDEY, J. and ET AL., *Nucl. Fusion* **43** (2003) 670.
- [17] MAINGI, R., TRITZ, K., FREDRICKSON, E., MENARD, J., and SABBAGH, S., *Nucl. Fusion* **45** (2005) 264.
- [18] KUGEL, H., MANSFIELD, D., MAINGI, R., and ET AL., *Journal of Nuclear Materials* **390-391** (2009) 1000.
- [19] BELL, M. G., KUGEL, H. W., KAITA, R., and ET AL., *Plasma Phys. Control. Fusion* **51** (2009) 124054.
- [20] CANIK, J. M., MAINGI, R., EVANS, T. E., and ET AL., *Phys. Rev. Lett.* **104** (2010) 045001.
- [21] MAINGI, R., OSBORNE, T. H., LEBLANC, B. P., and ET AL., *Physical Review Letters* **103** (2009) 075001.
- [22] SONTAG, A., CANIK, J. M., MAINGI, R., and ET AL., Pedestal characterization and stability of small-ELM regimes in NSTX submitted to *Nucl. Fusion* (2011).
- [23] LEBLANC, B. P., BELL, R. E., JOHNSON, D. W., et al., *Rev. Sci. Instrum.* **74** (2003) 1659.
- [24] BELL, R. E., ANDRE, R., KAYE, S. M., et al., *Phys. Plasmas* (2010) 082507.
- [25] OSBORNE, T. H., SNYDER, P. B., BURRELL, K. H., and ET AL., *J. Phys.: Conf. Ser.* **123** (2008) 012014.
- [26] GROEBNER, R. J. and OSBORNE, T. H., *Phys. Plasmas* **5** (1998) 1800.
- [27] GOHIL, P., MAHDAVI, M. A., LAO, L., and ET AL., *Phys. Rev. Lett.* **14** (1988) 1603.
- [28] WESSON, J. A., *Nucl. Fusion* **18** (1978) 87.
- [29] MANICKAM, J., *Phys. Fluids B* **4** (1992) 1901.
- [30] HEGNA, C. C., CONNOR, J. W., HASTIE, R. J., and WILSON2, H. R., *Phys. Plasmas* **3** (1996) 584.
- [31] KIRK, A., COUNSELL, G. F., CUNNINGHAM, G., et al., *Plasma Phys. Control. Fusion* **49** (2007) 1259.
- [32] MAGGI, C., GROEBNER, R., OYAMA, N., and ET AL., *Nucl. Fusion* **47** (2007) 535.
- [33] GROEBNER, R. J., OSBORNE, T. H., LEONARD, A. W., and FENSTERMACHER, M. E., *Nucl. Fusion* **49** (2009) 045013.
- [34] DIAMOND, P. H., LEBEDEV, V. B., NEWMAN, D. E., and CARRERAS, B. A., *Phys. Plasmas* **2** (1995) 3685.
- [35] MALKOV, M. A. and DIAMOND, P. H., *Phys. Plasmas* **15** (2008) 122301.
- [36] BURCKHART, A., WOLFRUM, E., FISCHER, R., et al., *Nucl. Fusion* **52** (2010) 105010.
- [37] SNYDER, P. B., WILSON, H. R., OSBORNE, T. H., and LEONARD1, A. W., *Plasma Phys. Control. Fusion* (46) A131.
- [38] SNYDER, P., AIBA, N., and ET AL., M. B., *Nucl. Fusion* **49** (2009) 085035.

- [39] SNYDER, P. B., GROEBNER, R. J., LEONARD, A. W., OSBORNE, T. H., and WILSON, H. R., *Phys. Plasmas* **16** (2009) 056118.
- [40] HUGHES, J. W., MOSSESIAN, D. A., HUBBARD, A. E., LABOMBARD, B., and MARMAR, E. S., *Phys. Plasmas* **9** (2002).
- [41] LINGERTAT, J., BHATNAGAR, V., CONWAY, G., et al., *Journal of Nuclear Materials* **266-269** (1999) 124 .
- [42] SAIBENE, G., HORTON, L., and R. SARTORI, E. A., *Nuclear Fusion* **39** (1999) 1133.
- [43] WILSON, H. R., SNYDER, P. B., HUYSMANS, G. T. A., and MILLER, R. L., *Phys. of Plasmas* **9** (2002) 1277.
- [44] SNYDER, P. B., WILSON, H. R., FERRON, J. R., and ET AL., *Phys. of Plasmas* **9** (2002) 2037.
- [45] SNYDER, P., *Gyrofluid Theory and Simulation of Electromagnetic Turbulence and Transport in Tokamak Plasmas*, PhD thesis, Princeton University, 1999.
- [46] BELLI, E. A. and CANDY, J., *Phys. of Plasmas* **17** (2010) 112314.
- [47] CROCKER, N. A., PEEBLES, W. A., KUBOTA, S., ZHANG, J., and FREDRICKSON, E. D., High resolution mhd mode structure measurements via multi-channel reflectometry in nstx, 52th Annual Meeting of the DPP-APS 2010. <http://meetings.aps.org/link/BAPS.2010.DPP.BP9.58>
- [48] NAZIKIAN, R., KRAMER, G. J., and VALEO, E., *Phys. of Plasmas* **8** (2001) 1840.
- [49] DIALLO, A. and SKIFF, F., *Phys. of Plasmas* **12** (2005) 110701.

The Princeton Plasma Physics Laboratory is operated  
by Princeton University under contract  
with the U.S. Department of Energy.

Information Services  
Princeton Plasma Physics Laboratory  
P.O. Box 451  
Princeton, NJ 08543

Phone: 609-243-2245  
Fax: 609-243-2751  
e-mail: [pppl\\_info@pppl.gov](mailto:pppl_info@pppl.gov)  
Internet Address: <http://www.pppl.gov>